

# Burnup analysis for the pebble-bed fluoride-salt-cooled high-temperature reactor based on the energy-dependent elastic scattering cross-sectional model

Zhi-Feng Li<sup>1,2</sup> · Jie-Jin Cai<sup>1</sup> · Qin Zeng<sup>1</sup> · Wen-Jie Zeng<sup>3</sup>

Received: 3 January 2018 / Revised: 14 March 2018 / Accepted: 19 March 2018 / Published online: 23 July 2018  
© Shanghai Institute of Applied Physics, Chinese Academy of Sciences, Chinese Nuclear Society, Science Press China and Springer Nature Singapore Pte Ltd. 2018

**Abstract** To carry out accurate burnup calculations for a pebble-bed fluoride-salt-cooled high-temperature reactor, the energy-dependent cross-sectional model based on the Doppler broadening rejection correction method has been proposed to develop the energy-dependent elastic scattering cross-sectional model. In this study, the Monte Carlo continuous energy code PSG2/Serpent was used to examine the difference between the constant cross-sectional model and the energy-dependent cross-sectional model during burnup. For the cases analyzed in this study, numerical simulations show that the multiplication coefficient was improved by hundreds pcm and <sup>239</sup>Pu concentration was improved by approximately 1–2% during burnup when the energy-dependent elastic scattering cross-sectional model is considered.

**Keywords** PB-FHR · Doppler broadening rejection correction · Resonance elastic scattering · PSG2/Serpent

---

This work was supported by the National Natural Science Foundation of China (Nos. 11675057 and 11705195), the Hunan Provincial Education Department Project of China (No. 15C1176), and the General Financial Grant from the China Postdoctoral Science Foundation (No. 2017M622697).

---

✉ Jie-Jin Cai  
chiven77@hotmail.com

<sup>1</sup> School of Electric Power, South China University of Technology, Guangzhou 510640, China

<sup>2</sup> School of Nuclear Engineering, Purdue University, West Lafayette, IN 47907, USA

<sup>3</sup> School of Nuclear Science and Technology, University of South China, Hengyang 421001, China

## 1 Introduction

Molten salt reactors (MSRs) have two main subtypes. In the first subtype, molten salt with dissolved nuclear fuel works as a moderator and fuel simultaneously; this subtype is traditionally identified as a liquid-fueled MSR. There were a few well-known working MSRs around the world, such as the molten salt reactor experiment (MSRE), the molten salt actinide recycler transforming system (MOSART), and the molten salt fast reactor (MSFR), which were developed in the USA, Russia and France, respectively. In the second subtype, molten salt works as a low-pressure coolant to a tristructural isotropic (TRISO)-fueled core; this subtype is traditionally identified as a pebble-bed fluoride-salt-cooled high-temperature reactor (PB-FHR) [1–3]. For example, the solid-fueled thorium molten salt reactor (TMSR-SF) is a variant of the PB-FHR; TMSR-SF was designed by the Shanghai Institute of Applied Physics for thorium-based nuclear energy utilization and hybrid nuclear energy application [4]. This work focuses on the burnup calculations of the PB-FHR-type pebble unit cell and the PB-FHR core by using the accurate elastic scattering models.

Elastic scattering models have three main subclasses. First subclass is the asymptotic model. In the asymptotic model, scattering is considered isotropic in the center-of-mass system [5]. The asymptotic model is basically accurate when the scattering processes occur at high incident neutron energy. However, in the lower incident neutron energy range, the asymptotic model is not accurate anymore because of ignoring the effects of target motion and forbidding up-scattering into the resonances of heavy nuclei [6]. Second subclass is the constant cross-sectional model (CXS). The CXS model was proposed to consider

the thermal motion of target nuclei during the elastic scattering events. The CXS model is known as the ideal gas model that has been frequently adopted in continuous energy Monte Carlo codes, such as MCNP4C and MCNP5 [7]. As distinct from the asymptotic model, up-scattering into the resonances of heavy nuclei is allowed in CXS model, and the speeds of the target nuclei are following the Maxwell–Boltzmann distribution [8]. In the sampling procedure, the scattering cross section at 0 K is set to a constant cross section. This assumption is reasonable for light target nuclei but not for heavy target nuclei [9]. Therefore, the third subclass known as energy-dependent cross-sectional model was proposed. When the incident neutron energy is close to the elastic scattering resonance peaks within the epithermal energy range, thermal motion of the nuclei would obviously influence the elastic scattering reaction rate and would lead to augment of neutron capture [10]; therefore, the energy-dependent cross-sectional model is used to take into account the resonant elastic scattering of the heavy target nuclei [11].

There are also three methods to consider the effects of energy-dependent scattering cross section in epithermal scattering process. The correctional methods for the energy-dependent scattering cross-sectional model are the  $S(\alpha, \beta)$  scattering law tables method, weight correction method (WCM) [12] and Doppler broadening rejection correction (DBRC) method. The  $S(\alpha, \beta)$  scattering law tables method is complex because it requires generation of  $S(\alpha, \beta)$  tables for each nuclide, and the tables should be generated on fine and unique energy grids [13]; WCM is slightly slower than the DBRC method [14]. Therefore, the DBRC method was adopted in this work to take the effects of an energy-dependent cross section into account.

This work is organized in the following manner: The implementation and validation of the DBRC method are described in Sect. 2. In Sect. 3, for the burnup calculation of the PB-FHR pebble unit cells and PB-FHR full core, comparison between the original CXS scattering kernel and the new DBRC scattering kernel is introduced. The final conclusion remarks are given in Sect. 4.

## 2 The implementation and validation of the DBRC method

### 2.1 Theory of the DBRC method

Standard CXS scattering kernel ignores the energy-dependent scattering cross section during sampling of the target velocity. But when the target nucleus is resonant, such as  $^{238}\text{U}$ , the CXS is not reasonable. The DBRC method [12] has been adopted in the latest continuous energy Monte Carlo code MCNP6 to consider the energy-

dependent elastic scattering cross section during the elastic scattering events [13]. The improved target probability density function in the DBRC method can be described as:

$$P(V, \mu | v_n) = C \left\{ \frac{\sigma_S(v_r, 0)}{\sigma_S^{\text{MAX}}(v_\xi, 0)} \right\} \left\{ \frac{v_r}{V + v_n} \right\} \{P_1 f_1(V) + P_2 f_2(V)\}, \quad (1)$$

$$C = \frac{(\sqrt{\pi}\beta v_n + 2)\sigma_S^{\text{MAX}}(v_r, 0)}{2\sqrt{\pi}\beta v_n \sigma_S^{\text{eff}}(v_n, T)}, \quad (2)$$

$$v_\xi \in \left[ v_n - \frac{4}{\sqrt{\alpha}}, v_n + \frac{4}{\sqrt{\alpha}} \right], \quad (3)$$

$$\alpha = \frac{M_t}{2k_B T}, \quad (4)$$

where  $v_n$  is the speed of incident neutron,  $v_r$  is the relative speed between incident neutron and target nucleus,  $M_t$  is the mass of target,  $V$  is the speed of the target,  $v_\xi$  is the dimensionless speed, and  $\sigma_S^{\text{MAX}}(v_\xi, 0)$  is the maximum value of elastic scattering cross sections within a range of the dimensionless speed determined by Eq. (3). In Eq. (1),  $\mu$  is uniformly sampled from  $[-1, 1]$ ,  $V$  is sampled from  $f_1(V)$  with probability  $P_1$  and from  $f_2(V)$  with probability  $P_2$ ,  $v_r/(V + v_n)$  and  $\sigma_S(v_r, 0)/\sigma_S^{\text{MAX}}(v_\xi, 0)$  are the first and second rejection test applied to the sampled velocity of the target. The energy-dependent scattering cross-sectional kernel model based on the DBRC method is implemented in PSG2/Serpent to accurately calculate the resonant elastic scattering of the heavy nuclei target.

### 2.2 Comparison of the DBRC and CXS for scattering kernel

$^{238}\text{U}$  is the most important heavy nuclei target because it has pronounced resonances in the elastic cross section in the epithermal range [9, 15–17]. Therefore, the first resonance of the  $^{238}\text{U}$  is analyzed in this section. Assuming an ideal case, the target material is a single nucleus of  $^{238}\text{U}$  in an infinite medium of constant density. The infinite medium is fixed at 1200 K, and the nuclear data library is based on ENDF/B-VII.0. Gray dashed line in Fig. 1a represents the monochromatic energy of the incident neutron, 6.52 eV, which is lower than the first elastic scattering resonance peak at 6.78 eV. The average emerging neutron energy distribution is also given in Fig. 1a. It can be found that both the CXS model and the energy-dependent scattering cross-sectional model based on DBRC method permit up-scattering. However, the probability of up-scattering in the DBRC method is higher than that in the CXS model, which means that more neutrons will be captured in the resonance peak of the  $^{238}\text{U}$ .

Gray dashed line in Fig. 1b represents the monochromatic energy of the incident neutron, 6.90 eV, which is

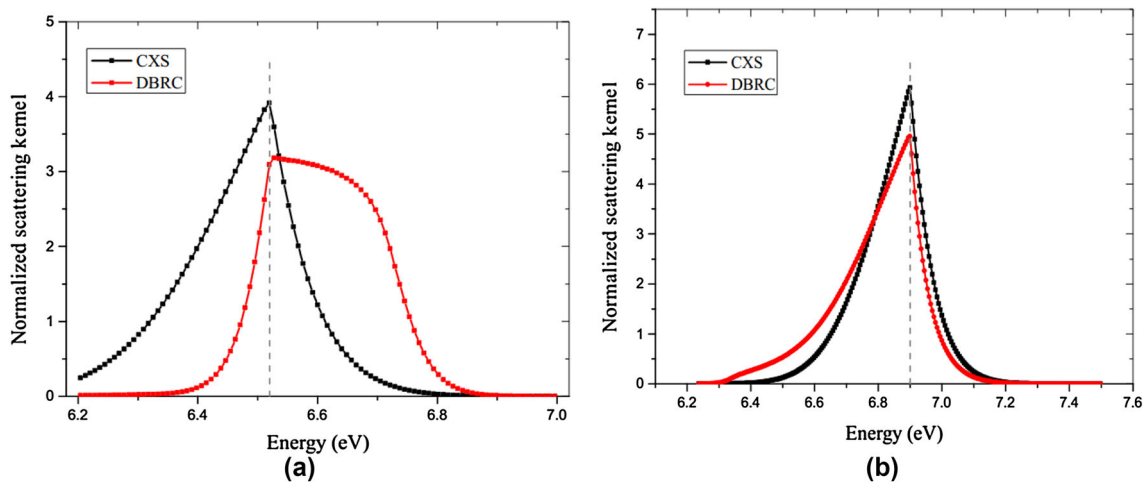


**Fig. 1** (Color online) Comparison of normalized elastic scattering kernels using CXS and DBRC on  $^{238}\text{U}$  with incident energy 6.52 eV (a) and 6.90 eV (b)

larger than the first elastic scattering resonance peak at 6.78 eV. The average emerging neutron energy distribution is also given in Fig. 1b. It can be found that the probability of down-scattering in the DBRC method is also higher than that in the CXS model, which means that more neutrons will be captured in the resonance peak of the  $^{238}\text{U}$ .

Based on the above phenomenon, we can predict that if the DBRC is used, the neutron capture will increase and the multiplication coefficient decreases in thermal reactors.

### 2.3 Validation of the DBRC method

Before the application of the DBRC method, the Mosteller benchmark problem [18] for LWR pin cell with UOX fuel and MOX fuel is adopted to validate the DBRC implemented in Monte Carlo code PSG2/Serpent [19]. The results calculated with the use of Monte Carlo code TRIPOLI-4 have been used for the comparison.

It was found that  $k_{\text{inf}}$  calculated by the TRIPOLI-4 and PSG2/Serpent agree well;  $k_{\text{inf}}$  decrease if the DBRC model is adopted. However, there are some minor deviations caused by different codes, different cycles, and other reasons. From Tables 1, 2, 3 and 4, compared with the results obtained by TRIPOLI-4, the energy-dependent scattering cross-sectional scattering model based on the DBRC method which is implemented in PSG2/Serpent can accurately calculate the resonance scattering. Therefore, the PSG2/Serpent code with DBRC method can be used to evaluate the resonant scattering effect of the PB-FHR.

## 3 Burnup calculation of the PB-FHR unit cell and PB-FHR core

The impact of the resonant elastic scattering effect within fuel was investigated with regard to PB-FHR pebble unit cells and PB-FHR full core. The detailed specifications of the coated particle, pebble, and coolant are given in Table 5.

### 3.1 PB-FHR unit cell

The PB-FHR pebble unit cell is composed of randomly distributed TRISO-coated fuel particles. In this work, the PB-FHR pebble unit cell was accurately modeled by the Monte Carlo code PSG2/Serpent using the explicit random geometric model [20, 21].

The impact of the energy-dependent scattering cross-sectional model based on DBRC method on the burnup calculation for the PB-FHR unit cell with different TRISO packing factors (TPFs) was investigated by performing two simulations: one with the original CXS scattering and another with the improved DBRC scattering. In the burnup calculation of the PB-FHR unit cell, temperatures of the fuel, coolant, and moderator were assumed to be 1200 K. Comparison of CXS and DBRC on the infinite multiplication factor during burnup for TPF = 7.03% can be observed in Fig. 2. The difference between CXS and DBRC on the infinite multiplication factor during burnup for TPF = 7.03% is also shown in Fig. 2; it can be found that the infinite multiplication factor decreases by 140~320 pcm during burnup if the DBRC is adopted. In addition, if the DBRC method is applied, more neutrons will be captured by  $^{238}\text{U}$ ; therefore, more  $^{239}\text{Pu}$  will be generated. The comparison of CXS and DBRC on the  $^{239}\text{Pu}$  concentration during burnup for TPF = 7.03% can be

**Table 1** Comparison of the TRIPOLI-4 and PSG2/Serpent for the UOX fuel at HZP

Enrichment (wt.%)	TRIPOLI-4			PSG2/Serpent		
	CXS	DBRC	$\Delta k/k$ (pcm)	CXS	DBRC	$\Delta k/k$ (pcm)
0.711	0.66599 (0.00004)	0.66537 (0.00004)	– 93	0.66647 (0.00002)	0.66612 (0.00002)	– 53
1.6	0.96182 (0.00004)	0.96091 (0.00004)	– 95	0.96153 (0.00002)	0.96092 (0.00002)	– 63
2.4	1.10016 (0.00005)	1.09909 (0.00005)	– 97	1.09941 (0.00002)	1.09885 (0.00002)	– 51
3.1	1.17817 (0.00005)	1.17711 (0.00005)	– 90	1.17744 (0.00002)	1.17683 (0.00002)	– 52
3.9	1.24084 (0.00005)	1.23962 (0.00005)	– 98	1.24017 (0.00002)	1.23936 (0.00002)	– 65
4.5	1.27619 (0.00005)	1.27508 (0.00005)	– 87	1.27554 (0.00002)	1.27491 (0.00002)	– 49
5.0	1.30045	1.29935	– 85	1.29836	1.29918	– 63

**Table 2** Comparison of the TRIPOLI-4 and PSG2/Serpent for the UOX fuel at HFP

Enrichment (wt.%)	TRIPOLI-4			PSG2/Serpent		
	CXS	DBRC	$\Delta k/k$ (pcm)	CXS	DBRC	$\Delta k/k$ (pcm)
1	0.66015 (0.00004)	0.65893 (0.00004)	– 185	0.66066 (0.00002)	0.65964 (0.00002)	– 155
2	0.95356 (0.00004)	0.95191 (0.00004)	– 173	0.95327 (0.00002)	0.95170 (0.00002)	– 165
4	1.09097 (0.00005)	1.08899 (0.00005)	– 181	1.09046 (0.00002)	1.08867 (0.00002)	– 164
6	1.26611 (0.00005)	1.26378 (0.00005)	– 184	1.26548 (0.00002)	1.26349 (0.00002)	– 157
8	1.29020	1.28800	– 171	1.28981	1.28768	– 165

**Table 3** Comparison of the TRIPOLI-4 and PSG2/Serpent for the MOX fuel at HZP

Enrichment (wt.%)	TRIPOLI-4			PSG2/Serpent		
	CXS	DBRC	$\Delta k/k$ (pcm)	CXS	DBRC	$\Delta k/k$ (pcm)
1	0.94809 (0.00004)	0.94697 (0.00004)	– 118	0.94543 (0.00002)	0.94455 (0.00002)	– 93
2	1.02701 (0.00004)	1.02576 (0.00004)	– 122	1.02152 (0.00002)	1.02051 (0.00002)	– 99
4	1.08539 (0.00004)	1.08421 (0.00004)	– 109	1.07706 (0.00002)	1.07579 (0.00002)	– 118
6	1.11527 (0.00005)	1.11418 (0.00005)	– 98	1.10550 (0.00002)	1.10482 (0.00002)	– 62
8	1.13911	1.13803	– 95	1.12828	1.12920	– 82

observed in Fig. 3. The difference between CXS and DBRC on the  $^{239}\text{Pu}$  concentration during burnup for TPF = 7.03% is also shown in Fig. 3; it can be found that the  $^{239}\text{Pu}$  concentration increases by 1.2–1.6% during burnup if the DBRC is adopted, that is to say, the

computational accuracy of the  $^{239}\text{Pu}$  concentration increases by 1.2–1.6%.

Similarly, comparison of CXS and DBRC on the infinite multiplication factor during burnup for TPF = 15% can be observed in Fig. 4. The difference between CXS and DBRC on the infinite multiplication factor during burnup

**Table 4** Comparison of the TRIPOLI-4 and PSG2/Serpent for the MOX fuel at HFP

Enrichment (wt.%)	TRIPOLI-4			PSG2/Serpent		
	CXS	DBRC	$\Delta k/k$ (pcm)	CXS	DBRC	$\Delta k/k$ (pcm)
1	0.93857 (0.00004)	0.93642 (0.00004)	– 229	0.93601 (0.00002)	0.93412 (0.00002)	– 155
2	1.01615 (0.00004)	1.01393 (0.00004)	– 218	1.01045 (0.00002)	1.00870 (0.00002)	– 202
4	1.07376 (0.00004)	1.07156 (0.00004)	– 205	1.06528 (0.00002)	1.06311 (0.00002)	– 204
6	1.10339 (0.00005)	1.10139 (0.00005)	– 181	1.09378 (0.00002)	1.09187 (0.00002)	– 175
8	1.12736	1.12530	– 183	1.11746	1.11558	– 168

**Table 5** Primary parameters of the PB-FHR

Parameters	Value
General parameters	
Cylindrical core diameter (cm)	135
Initial loading height (cm)	130
Thickness of top reflector (cm)	63.2
Thickness of side reflector (cm)	75
Thickness of bottom reflector (cm)	56.8
Thickness of vessel (cm)	2
Volume packing fraction of the fuel pebbles in the core (%)	60
Fuel pebble	
Diameter of fuel pebble (cm)	3
Diameter of fuel region in the fuel pebble (cm)	2.5
Density of graphite in the shell and matrix (g/cm <sup>3</sup> )	1.73
Enrichment of <sup>235</sup> U (weight) (%)	17
Weight of heavy metal uranium in each pebble (g)	7
Volume packing fraction of the particles in the pebble (%)	7.03–30
TRISO particle	
Radius of the fuel kernel (cm)	0.025
UO <sub>2</sub> density of kernel (g/cm <sup>3</sup> )	10.4
Coating layer material (starting from kernel)	PyC/IPyC/SiC/OPyC
Coating layer thickness (cm) (starting from kernel)	0.009/0.004/0.0035/0.004
Coating layer density (g/cm <sup>3</sup> ) (starting from kernel)	1.1/1.9/3.18/1.9
Coolant	
Enrichment of <sup>6</sup> Li in 2LiF-BeF <sub>2</sub> (%)	0.005

for TPF = 15% is shown in Fig. 4; it can be found that the infinite multiplication factor decreases by 400–570 pcm during burnup if the DBRC is adopted. In addition, comparison of CXS and DBRC on the <sup>239</sup>Pu concentration during burnup for TPF = 15% can be observed in Fig. 5. The difference between CXS and DBRC on the <sup>239</sup>Pu concentration during burnup for TPF = 15% is shown in Fig. 5 too; it can be found that the <sup>239</sup>Pu concentration increases by 1.4–2.2% during burnup if the DBRC is adopted.

In addition, comparison of CXS and DBRC on the infinite multiplication factor during burnup for TPF = 30% can be observed in Fig. 6. The difference between CXS and DBRC on the infinite multiplication factor during burnup for TPF = 30% is shown in Fig. 6; it can be found that the infinite multiplication factor decreases by 360–730 pcm during burnup if the DBRC is adopted. In addition, comparison of CXS and DBRC on the <sup>239</sup>Pu concentration during burnup for TPF = 30% can be observed in Fig. 7. The difference between CXS and DBRC on the <sup>239</sup>Pu concentration during burnup for

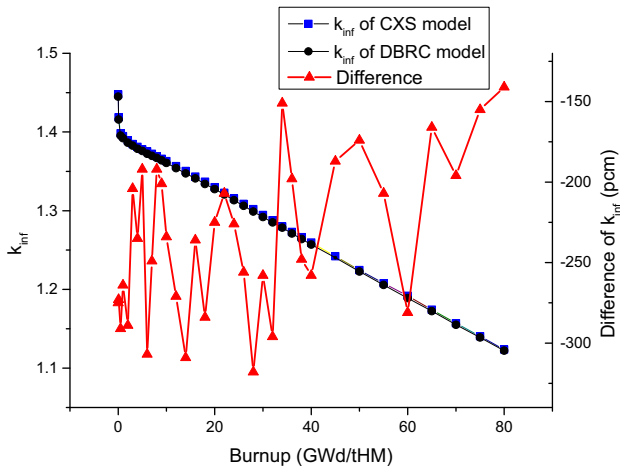


**Fig. 2** (Color online) Comparison of  $k_{inf}$  during burnup for the unit cell with TPF = 7.03%

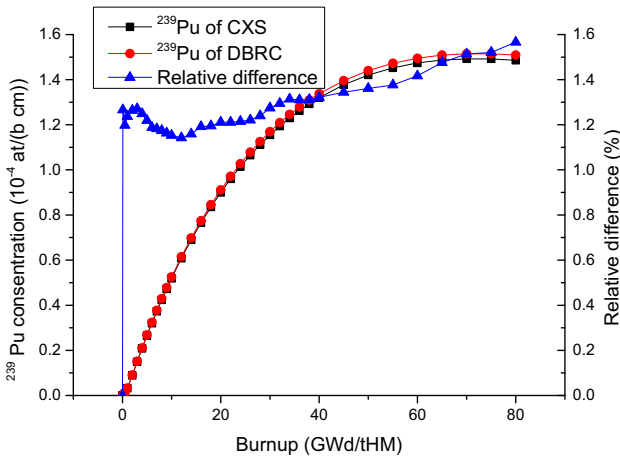


**Fig. 3** (Color online) Comparison of  $^{239}\text{Pu}$  concentration during burnup for the unit cell with TPF = 7.03%

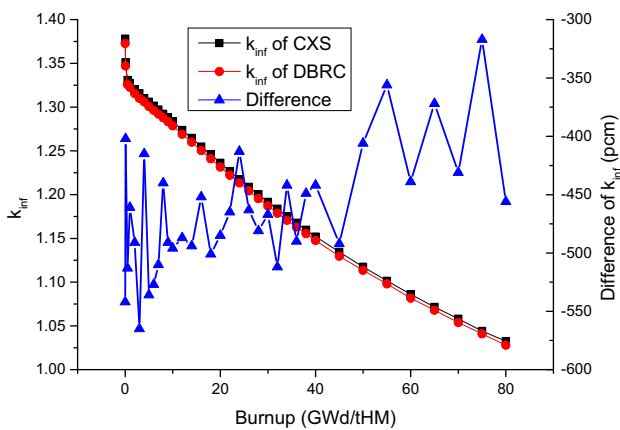


**Fig. 4** (Color online) Comparison of  $k_{inf}$  (a) during burnup for the unit cell with TPF = 15%

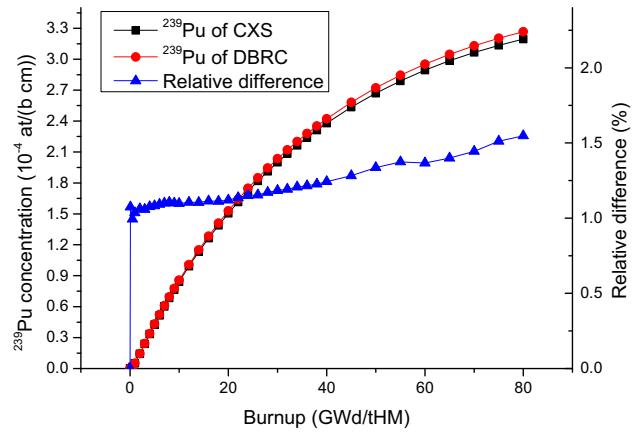


**Fig. 5** (Color online) Comparison of  $^{239}\text{Pu}$  concentration during burnup for the unit cell with TPF = 15%

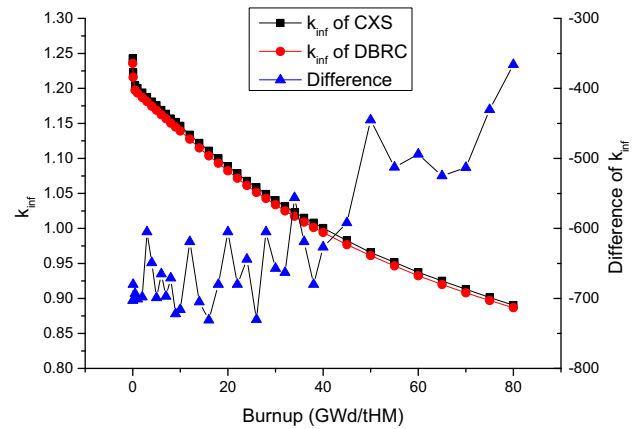


**Fig. 6** (Color online) Comparison of  $k_{inf}$  during burnup for the unit cell with TPF = 30%

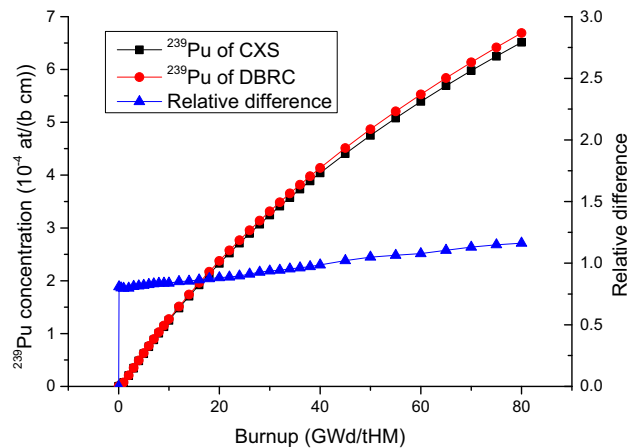


**Fig. 7** (Color online) Comparison of  $^{239}\text{Pu}$  concentration during burnup for the unit cell with TPF = 30%

TPF = 30% is also shown in Fig. 7; it can be found that the <sup>239</sup>Pu concentration increases by 1.9–2.7% during burnup if the DBRC is adopted.

### 3.2 PB-FHR full core

The PB-FHR is composed of randomly distributed fuel pebbles which consist of fully randomly distributed TRISO-coated fuel particles; the PB-FHR full core is accurately modeled by the Monte Carlo code PSG2/Serpent using the random geometric model.

The impact of the energy-dependent scattering cross-sectional model based on the DBRC method on the burnup calculation for the PB-FHR full core with TPF = 7.03% is investigated by performing two simulations: one with the original CXS scattering and another with the improved DBRC scattering. In the burnup calculation of the PB-FHR full core, temperatures of the fuel, coolant, and moderator are assumed to be 1200 K. Comparison of CXS and DBRC on the effective multiplication factor during burnup can be observed in Fig. 8. The difference between CXS and DBRC on the effective multiplication factor during burnup for the PB-FHR full core is shown in Fig. 8; it can be found that the effective multiplication factor decreases by 144~205 pcm during burnup if DBRC is adopted. In addition, comparison of CXS and DBRC on the <sup>239</sup>Pu concentration during burnup for the PB-FHR full core can be observed in Fig. 9. The difference between CXS and DBRC on the <sup>239</sup>Pu concentration during burnup for the PB-FHR full core is also shown in Fig. 9; it can be found that the <sup>239</sup>Pu concentration increases by 1.1–1.3% during burnup if DBRC is adopted.

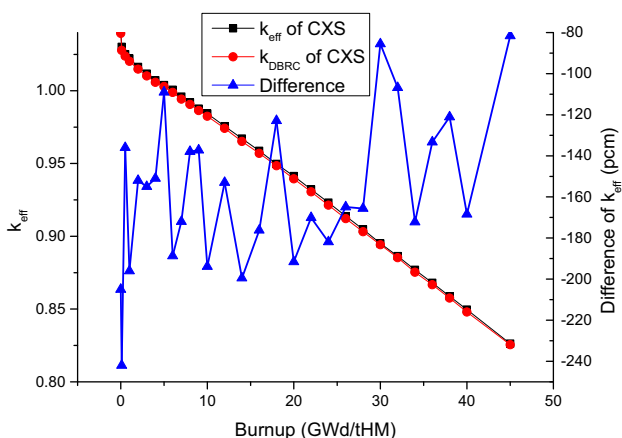


**Fig. 8** (Color online) Comparison of  $k_{eff}$  during burnup for the PB-FHR full core

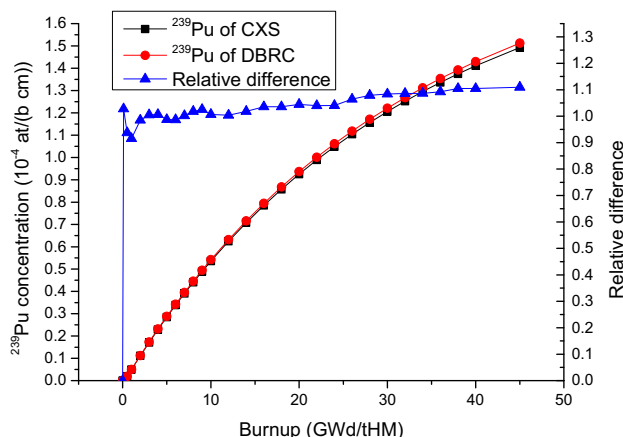


**Fig. 9** (Color online) Comparison of <sup>239</sup>Pu concentration during burnup for the PB-FHR full core

## 4 Conclusion

The energy-dependent scattering cross-sectional model based on the DBRC method was studied. If the energy of incident neutron is close to the resonance peaks of <sup>238</sup>U, there are obvious differences between CXS and DBRC. Compared with the CXS model, enhanced neutron up-scattering and down-scattering toward the resonance peaks were observed when the DBRC method was adopted, which means that more neutrons would be captured by the <sup>238</sup>U and more <sup>239</sup>Pu will be generated in the burnup. For the pebble unit cell with TPF = 7.03%, the traditional CXS model underestimates the  $k_{inf}$  and <sup>239</sup>Pu concentration by 140–320 pcm and 1.2–1.6%, respectively. For the pebble unit cell with TPF = 15%, the traditional CXS model underestimates the  $k_{inf}$  and <sup>239</sup>Pu concentration by 400–570 pcm and 1.4–2.2%, respectively. For the pebble unit cell with TPF = 15%, the traditional CXS model underestimates the  $k_{inf}$  and <sup>239</sup>Pu concentration by 360~730 pcm and 1.9–2.7%, respectively. Burnup calculation of the PB-FHR unit cells shows that the difference of  $k_{inf}$  and <sup>239</sup>Pu concentration caused by the DBRC approximately augments with the increasing TPF.

In addition, the difference between the CXS and the DBRC for the PB-FHR full core was studied. The traditional CXS model underestimates the  $k_{eff}$  and <sup>239</sup>Pu concentration by 144–205 pcm and 1.1–1.3%, respectively. The difference for the PB-FHR full core is non-negligible. Therefore, the impact of the energy-dependent scattering cross-sectional model needs to be considered during the burnup calculation for the 10-MW TMSR-SF.

## References

1. D.L. Zhang, L.M. Liu, M. Liu et al., Review of conceptual design and fundamental research of molten salt reactors in China. *Int. J. Energy Res.* **1**, 1–15 (2018). <https://doi.org/10.1002/er.3979>
2. L.M. Liu, D.L. Zhang, Q. Lu et al., Preliminary neutronic and thermal-hydraulic analysis of a 2 MW Thorium-based molten salt reactor with solid fuel. *Prog. Nucl. Energy* **86**, 1–10 (2016). <https://doi.org/10.1016/j.pnucene.2015.09.011>
3. C. Forsberg, The advanced high-temperature reactor: high-temperature fuel liquid salt coolant, liquid-metal-reactor plant. *Prog. Nucl. Energy* **47**, 32–43 (2005). <https://doi.org/10.1016/j.pnucene.2005.05.002>
4. Z.M. Dai, Thorium molten salt reactor nuclear energy system (TMSR). *Molten Salt React. Thorium Energy* **1**, 521–540 (2017). <https://doi.org/10.1016/B978-0-08-101126-3.00017-8>
5. J.J. Duderstadt, L.J. Hamilton, *Nucl. React. Anal.* (Wiley, New York, 1976), pp. 12–34
6. M. Ouisloumen, R. Sanchez, A model for neutron scattering off heavy isotopes that accounts for thermal agitation effects. *Nucl. Sci. Eng.* **107**, 189–200 (1991). <https://doi.org/10.13182/NSE89-186>
7. X-5 Monte Carlo Team, MCNP A General Monte Carlo N-Particle Transport Code (Los Alamos National Laboratory, New Mexico, 2008), (pp. 10–25)
8. D.E. Cullen, C.R. Weisbin, Exact Doppler broadening of tabulated cross sections. *Nucl. Sci. Eng.* **60**, 199–229 (1976). <https://doi.org/10.13182/NSE76-1>
9. D. Lee, K. Smith, J. Rhodes, The impact of  $^{238}\text{U}$  resonance elastic scattering approximations on thermal reactor Doppler reactivity. *Ann. Nucl. Energy* **36**, 274–280 (2009). <https://doi.org/10.1016/j.anucene.2008.11.026>
10. R. Dagan, On the use of  $S(\alpha, \beta)$  tables for nuclides with well pronounced resonances. *Ann. Nucl. Energy* **32**, 367–377 (2005). <https://doi.org/10.1016/j.anucene.2004.11.003>
11. A. Zoia, E. Brun, C. Jouanne et al., Doppler broadening of neutron elastic scattering kernel in TRIPOLI-4. *Ann. Nucl. Energy* **54**, 218–226 (2013). <https://doi.org/10.1016/j.anucene.2012.11.023>
12. T. Mori, Y. Nagaya, Comparison of resonance elastic scattering models newly implemented in MVP continuous-energy monte carlo code. *J. Nucl. Sci. Technol.* **46**, 793–798 (2009). <https://doi.org/10.1080/18811248.2007.9711587>
13. J.A. Walsh, B. Forget, S.S. Kord, Accelerated sampling of the free gas resonance elastic scattering kernel. *Ann. Nucl. Energy* **69**, 116–124 (2014). <https://doi.org/10.1016/j.anucene.2014.01.017>
14. T.H. Trumbull, T.E. Fieno, Effects of applying the Doppler broadened rejection correction method for LEU and MOX pin cell depletion calculations. *Ann. Nucl. Energy* **62**, 184–194 (2013). <https://doi.org/10.1016/j.anucene.2013.06.013>
15. B. Becker, R. Dagan, C.H.M. Broeders, Improvement of the resonance scattering treatment in MCNP in view of HTR calculations. *Ann. Nucl. Energy* **36**, 281–285 (2009). <https://doi.org/10.1016/j.anucene.2008.12.009>
16. E.E. Sunny, F.B. Brown, B.C. Kiedrowski et al., Temperature effects of resonance scattering for epithermal neutrons in mcnp, in: PHYSOR 2012, Knoxville, Tennessee, USA, April 15–20, 2012
17. Z.F. Li, L.Z. Cao, H.C. Wu et al., The impacts of thermal neutron scattering effect and resonance elastic scattering effect on FHRs. *Ann. Nucl. Energy* **97**, 102–114 (2016). <https://doi.org/10.1016/j.anucene.2016.07.014>
18. R.D. Mosteller, *Computational Benchmarks for the Doppler Reactivity Defect* (Los Alamos National Laboratory, New Mexico, 2006), pp. 1–8
19. J. Leppänen, *PSG2/PSG2/Serpent—a continuous-energy monte carlo reactor physics burnup calculation code* (VTT Technical Research Centre, Finland, 2004), pp. 1–153
20. Z.F. Li, L.Z. Cao, H.C. Wu, The impacts of random effect and scattering effects on the neutronics analysis of the PB-FHR. *Ann. Nucl. Energy* **108**, 163–171 (2017). <https://doi.org/10.1016/j.anucene.2017.04.044>
21. Z.F. Li, L.Z. Cao, H.C. Wu et al., On the improvements in neutronics analysis of the unit cell for the pebble-bed fluoride-salt-cooled high-temperature reactor. *Prog. Nucl. Energy* **93**, 287–296 (2016). <https://doi.org/10.1016/j.pnucene.2016.09.004>